Comparative numerical analysis of the posterior and anterior behind armour blunt trauma using GHBMC M50-P model

Patrick Matt, Marcin Jenerowicz, Matthias Boljen

Abstract Behind armour blunt trauma (BABT) has been investigated in depth for anterior impacts, but there are only a few studies regarding posterior BABT. The objective of this study is the numerical analysis of posterior BABT and the comparison to anterior BABT using the GHBMC M50-P. Two posterior impacts (vertebra *T7* and between 9th and 10th rib) are compared to two anterior impacts (mid-sternum and 5th rib) by evaluating the body wall deformations and the strains in hard tissues, such as ribs, vertebrae and sternum. Using a substitute impact layer (SIL) to imprint the back face deformation (BFD) and adapting each impact profile individually, it was possible to investigate these impact positions with an equal energy input. Depending on the impacted position, the imprinting of BFD with the SIL-method results in different magnitudes of body wall displacements, with different internal structures being subjected to varying levels of stress. The anterior impacts result in critical strain values in sternum, costal cartilage and ribs, while the posterior impacts result in critical values in ribs and vertebrae. The comparison of both posterior positions with their respective anterior positions reveals higher rib strains in both posterior cases.

Keywords Behind armour blunt trauma, finite element analysis, human body model, injury assessment, posterior impact.

I. INTRODUCTION

Projectiles impacting protective armour without perforation can cause the wearer behind armour blunt trauma (BABT). BABT is caused by the rapid deformation of the body armour and the resulting energy transfer to the human body [1]. Among the reported BABT cases are injuries such as skin contusions and perforations, rib and sternal fractures, and contusions to internal organs, including lung and spleen [1-5].

According to the current test standard for the ballistic resistance of body armour of the National Institute of Justice (NIJ), the back face deformation (BFD) of a body armour into a Roma Plastilina No.1 clay block impacted by a specific test round with a specific velocity, representing a certain threat level, may not exceed an indention limit of 44 mm [6-7]. If the maximum BFD depth is less than 44 mm, the armour passes. This limit originates from ballistic experiments conducted on goats in 1976 [8]. By recreation of BABT field cases, Bir *et al*. correlated sustaining a severe injury with a probability of 50% with a BFD of 43.6 mm, which is close to the NIJ limit [2]. However, the 44 mm limit is often criticised due to the fact that it only provides a pass/fail criterion and it does not take into account the thoracic region-specific injury tolerances, i.e. the human body is seen as a homogeneous entity [9-11].

Most of the experimental studies focus primarily on anterior BABT [10][12-15]. There are only a few experimental investigations regarding posterior BABT, which have been summarised to the author's best knowledge in Table I. These studies vary widely in their setup with regard to projectile, body armour and impacted specimen (Table I). But what all studies have in common is that they focus their investigations on spinal impacts. Most reported injuries include bony damage to the vertebra without evidence of spinal cord damage, while Zhang *et al*. reported neural damage to the spinal cord and brain without any bony injuries [8][15-19]. Furthermore, Bass *et al*. compared a midsternal impact with a spinal impact in a post-mortem human subject (PMHS) experiment, and pointed out that anterior BABT may not be the worst case due to the higher injury level in the spinal impact and that further investigations in the area of spinal impacts could be of high significance [15].

P. Matt (e-mail: patrick.matt@emi.fraunhofer.de; tel: +497612714437) and M. Jenerowicz are Research Assistants and M. Boljen is Head of the Research Group Human Body Dynamics at Fraunhofer Institute for High-Speed Dynamics, Ernst-Mach-Institute, EMI, Freiburg, Germany.

Besides experimental research, BABT is also being studied through the use of computational methods. In finite element (FE) simulations, human body models (HBMs) are subjected to non-penetrating BABT loadings, and the effects on internal structures, including the ribs, sternum and lungs, are evaluated [20-22]. A challenging aspect of investigating BABT in FE simulations is the donning of protective armour on HBMs [23-24]. These BABT studies also focus on anterior cases, while posterior impacts are not considered [20-22].

The objective of this study is the numerical analysis of posterior BABT and the comparison to anterior BABT using the GHBMC M50-P. Two posterior impacts (vertebra *T7* and between 9th and 10th rib) will be compared to two anterior impacts (mid-sternum and 5th rib) by evaluating the body wall deformations and the strains in hard tissues, such as ribs, vertebrae and sternum.

TABLE I
EXPERIMENTAL STUDIES REGARDING POSTERIOR BABT OVER THE SPINE (BASED ON [19]). VALUES WITH * ARE ESTIMATED

Projectile	Body Armour	Specimen	Injuries	Source
Round: 0.38 calibre v = 244 m/s m = 10.24 g E_{kin} = 305 J	7-ply, 14-inch square of Kevlar® 29	7 anaesthetised goats (approx. 40 kg)	Soft tissue wounds, fractured spinous processes, no spinal cord injury	Goldfarb *et al*. 1975 [8], Soderstrom *et al*. 1978 [16]
Round: 7.62 mm v = 698 m/s m = 9.72 g E_{kin} = 2368 J	Ultra-high molecular weight polyethylene (UHMWPE) body armour	PMHS (female, 70 years old, 54 kg)	Laceration between thoracic vertebrae and disintegration of spinous processes down to the spinal canal (AIS5 injury)	Bass *et al*. 2006 [15]
Round: 5.56 mm v_{mean} = 910 m/s m* = 4 g E_{kin}* = 1656 J	Ceramic plate combined with polyethylene body armour	28 anaesthetised pigs (42–61 kg)	Damage to skin, lung, spinal cord and brain, no broken vertebrae	Zhang *et al*. 2011 [17]
Round: 9 mm Luger v_{mean} = 373 m/s m* = 8 g E_{kin}* = 557 J	Soft armour	Cadaveric pig torso (65 kg)	Soft tissue wounds, spinous process fracture, no spinal canal/cord damage	Jennings *et al*. 2018 [18]
Round: 7.62 NATO v_{mean} = 838 m/s m* = 9.6 g E_{kin}* = 3371 J	Hard armour plates combined with soft armour	Cadaveric pig torso (65 kg)	No bony injuries and no spinal canal/cord damage; rib shot: rib fracture	Jennings *et al*. 2018 [19]

II. METHODS

HBM and Armour

The GHBMC M50 Detailed Pedestrian v5.3.4 Model was selected as the HBM and all implemented options for strain-based element deletion were deactivated [25]. The GHBMC M50-P model was combined with a soft ballistic body armour using a forming simulation [24]. The material parameters for the Kevlar® vest were adopted from Ivanov and Tabiei [26]. The armour consisted of three fabric packages, holding 13, 14 and 13 single plies. The plies were sewn together at the edges. Each plie was 0.28 mm thick and the plies were oriented in alternating directions of 0°/90° and ±45° [24]. Depending on the impacted side of the body, anterior or posterior, the body armour was either only donned on the front or the back of the model.

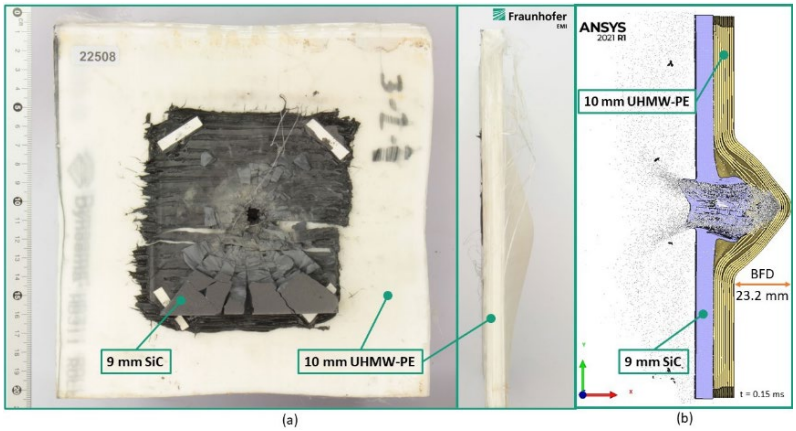

Fig. 1. (a) Hard-ballistic plate of 9 mm silicon carbide (SiC) and 10 mm of UHMWPE after impact with 7.62 mm x 51 AP8-Projectile at v_P=913 m/s; (b) corresponding simulation of the performed experiment with Ansys-Autodyn, max. BFD 23.2 mm at 0.15 ms [21].

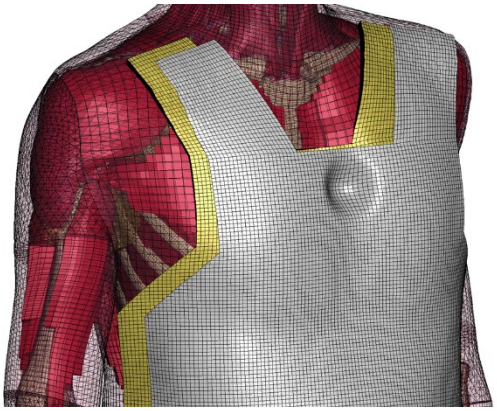

Fig. 2. GHBMC with ballistic armour (yellow), and SIL (grey) deforming at mid-sternal level. For illustration purposes the SIL was offset from the armour.

Impact Condition and Positions

A load case from previous studies was selected for the present research [21][24]. This load case was based upon a non-penetrating BFD of an armour-piercing projectile impact with a striking velocity of 913 m/s on a hard-ballistic plate without backing (Fig. 1a). The time-displacement profile of the BFD was measured using a high-speed camera (frame rate: 125 kHz). It should be noted that the addition of a backing material would have probably reduced the severity of the impact. The experimental BFD of the UHMWPE composite was recreated in an Ansys-Autodyn simulation (Fig. 1b). From this simulation the time history of the nodal displacements of the BFD was extracted until t=0.15 ms with a maximum BFD of 23.2 mm. The BFD time-displacement-history was transferred into the LS-DYNA environment by introducing a rigid substitute impact layer (SIL), which would reproduce the deformation profile of the BFD at a specified location onto the soft body armour by kinematic constraints. In other words, this means that selected nodes of SIL replicate the BFD of the UHMWPE through an imposed motion and deform the underlying soft armour through a contact definition. SIL was modelled as a layer on top of the soft armour, which had the advantage that the locations of the impact zones could be easily varied, the distance between SIL and armour was at every point constant and the vector of the deformation profile was always orthogonal to the elements of the vest and thus directed into the body. Furthermore, modelling the impact with SIL had also the advantage that it replaces the impacting projectile and the fragmenting hard armour plate and therefore, the need to model these with an extremely fine discretisation. Figure 2 shows the GHBMC with the soft body armour and SIL imprinting an impact profile at mid-sternal level onto the armour. Contact definitions were established between the GHBMC and the armour model, and between the armour model and SIL.

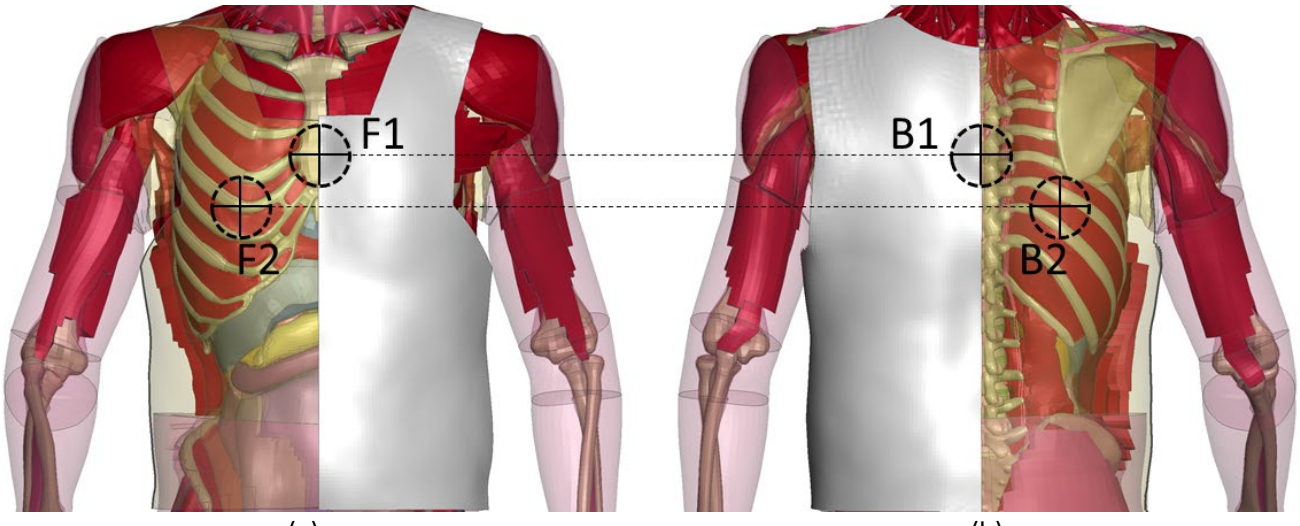

Fig. 3. Overview of impact positions on GHBMC with a half-blanked SIL (grey) and a transparent body armour. (a) Positions *F1* and *F2* on the anterior side. (b) Positions *B1* and *B2* on the posterior side.

Two impact positions were chosen on the front at the mid-sternum (*F1*) and at the transition area of the right 5th rib to the costal cartilage (*F2*). The posterior points were obtained by mirroring the anterior positions at the coronal plane of the GHBMC to the back, being therefore on level with the 7th thoracic vertebra (*B1*) and between the 9th and 10th rib on the dorsal right side (*B2*). The impact positions are shown in Figure 3.

In comparison to the previous studies, the deformation profile of SIL was modified for each impact position individually, with the aim of an equal external energy input of 264 J. Imprinting the initial SIL profile with a depth of 20 mm and a diameter of 70 mm over a period of 150 µs resulted, depending on the impact position, in a wide range of different external energy values (Fig. 4 and Fig. 5). By running a pre-simulation for each position with the initial SIL profile, it was possible to identify the time at which an external energy of 264 J was reached and to identify the final node positions of SIL for each case, which were then used in the following simulations as individual profiles. The value of 264 J was determined by extracting the mass and velocity of the debris from the above-mentioned Ansys-Autodyn simulation [21]. Here, the nodes of the projectile and hard armour ceramic plate were identified, which were significantly transmitting the impulse to the soft armour. These nodes had a total mass of 41 g and would hit the soft armour with a remaining mean velocity of *v*=113.4 m/s, resulting in a kinetic energy of 264 J. The modified profiles for each position are shown in Figure 5. All simulations were conducted with LS-DYNA version R12. Each impact was investigated for 3 ms.

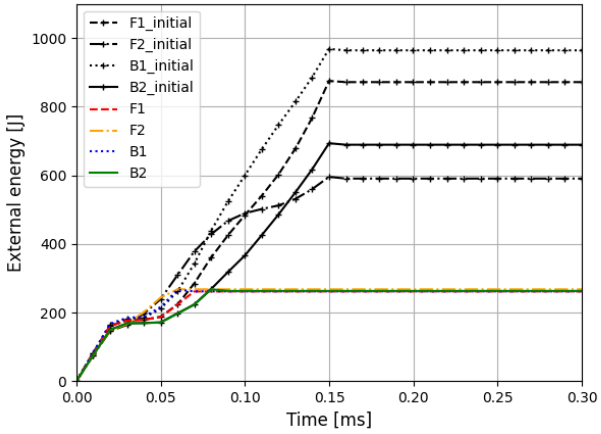

Fig. 4. External energy over time: each initial BFD profile has been limited to an external energy limit of 264 J.

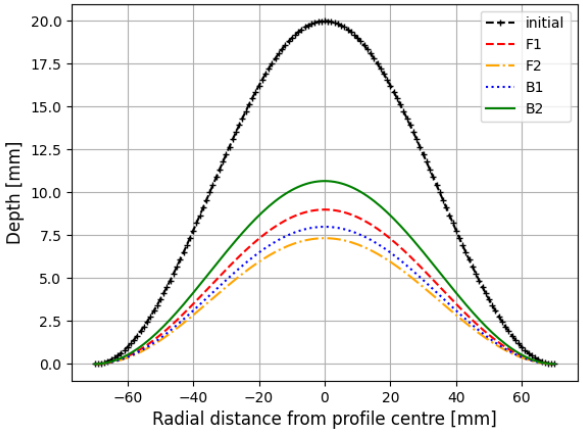

Fig. 5. Adapted BFD profiles with an external energy limitation of approx. 264 J for position *F1* (dashed red), *F2* (dash-dotted orange), *B1* (dotted blue) and *B2* (solid green). The initial profile is shown as black dotted line.

Evaluation

The deformation of the HBM was investigated by analysing the maximum body wall displacement (BWD) and the maximum value of the viscous criterion (VC) [27]:

$$VC = \max(v(t) * c(t)) \quad (1)$$

where *v(t)* is the time-dependent deformation velocity of the thorax and *c(t)* the time-dependent compression of the thorax. *c(t)* is calculated by dividing the maximum skin displacement by the thorax thickness. To evaluate these kinetic values, a mean value was computed based on five nodes. This involved identifying the node with the maximum value and calculating the mean value using the four nearest nodes.

Furthermore, the strains in the cortical areas of the ribs and vertebrae were analysed and the maximum strains and the volumetric fraction (VF) of the ribs and vertebrae, which have exceeded a certain strain threshold over the total impact time, were determined. This approach was chosen for the evaluation of the ribs and vertebrae to provide a more quantitative and comparative analysis rather than solely relying on maximum values and qualitative observations.

In the ribs, the maximum principal strains were determined, and a threshold of 1.57% was chosen for the VF. The limit of 1.57% for the $VF_{1.57}$ is based on the study of Agnew *et al.*, who reported a peak tensile strain of

1.5725% at failure in the ribs of young adults [28]. The critical loaded vertebrae were investigated regarding the maximum effective strains. Due to the lack of available data regarding the fracture of vertebrae in the scenario of a horizontal high-speed impact, a threshold value from Somasundaram *et al*. was selected for the indication of possible damage. Somasundaram *et al*. correlated an effective strain of 1.37% in the anterior side of the vertebral body of an GHBMC M50 with a vertebral body fracture in a PMHS test in the event of an underbody blast [29]. Therefore, it was assumed that damage could occur in the vertebrae after an effective strain of 1.37% was reached. It should be noted that this value has to be used with caution because the loading conditions of an under body blast and a direct horizontal impact vary widely.

III. RESULTS

As shown in Table II, the external energy limit of 264 J could be obtained by customising the SIL profile for each impact zone individually. The values deviated within an acceptable range of -0.76–1.89% from the target value of 264 J. The energy limitation resulted in maximum BFD of the SIL with values between 7.33 mm and 10.67 mm. The lowest BFD could be observed for *F2* (7.33 mm), while the highest value occurred for *B2* (10.67 mm), which was 45.6% greater than the BFD at *F2*.

TABLE II
MAXIMUM EXTERNAL ENERGY, BFD OF SIL, MAXIMUM BODY WALL DISPLACEMENT AND VCMAX

Position	External Energy [J]	BFD SIL [mm]	BWD [mm]	VC_{max} [m/s]
F1	267	9.0	16.52	2.33
F2	266	7.33	32.16	4.39
B1	262	8.0	24.18	3.28
B2	269	10.67	11.68	1.95

The maximum BWD values ranged from 11.68 mm up to 32.16 mm (Table II). The highest BWD occurred at the anterior position *F2* and the lowest at the posterior position *B2*. All maximum displacement values are below the NIJ threshold of 44 mm for an impact in clay. The maximum BWD correlated positively with the VC_{max} values (Fig. 6), which was to be expected according to Equation (1). The VC profiles over time are shown in Figure 7. The lowest value of VC_{max} was observed at *B2* with 1.95 m/s and the highest value at *F2* with 4.39 m/s (Table II). According to Bir *et al*., a VC_{max} of 0.8 m/s during an anterior ballistic impact would result in a 50% probability of sustaining a thoracic skeletal injury of AIS2 or AIS3, while a VC_{max} of approximately 1.8 m/s would indicate a 100% chance [14]. Comparing the maximum BWD and VC_{max}, no general tendency can be observed between anterior and posterior cases for the limited number of impact positions.

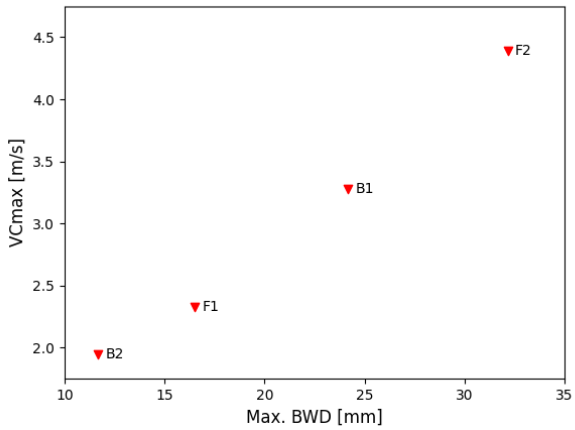

Fig. 6. VC_{max} over maximum BWD.

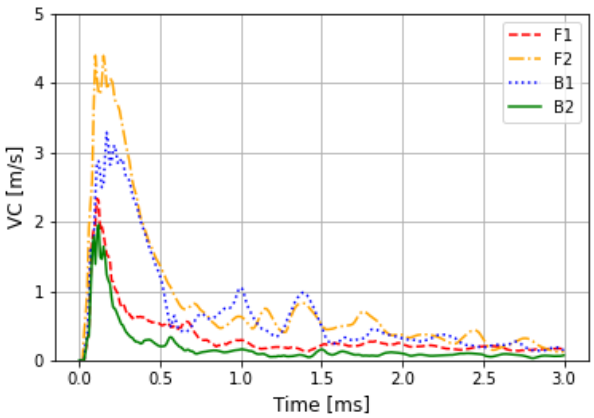

Fig. 7. VC over time.

In Figure 8 the maximum principal strains in the structures of the thorax (sternum, costal cartilage, ribs, and vertebrae) are shown for each impact position. In the anterior impacts (Fig. 8a and Fig. 8c), primarily the sternum, the ribs and the connecting costal cartilage are affected. At *F1* (Fig. 8a) and also at *F2* (Fig. 8c) strains above 2.0% could be observed in the costal cartilage, indicating as per material model of the GHBMC possible damage to this structure. The sternum exhibited the highest strains when directly loaded at *F1*, with strains exceeding 2.0% detected within the first hundred microseconds, which would result in element failure according to the associated material model. Compared to the anterior cases, the posterior conditions mainly impacted the vertebrae and ribs (Fig. 8b and Fig. 8d).

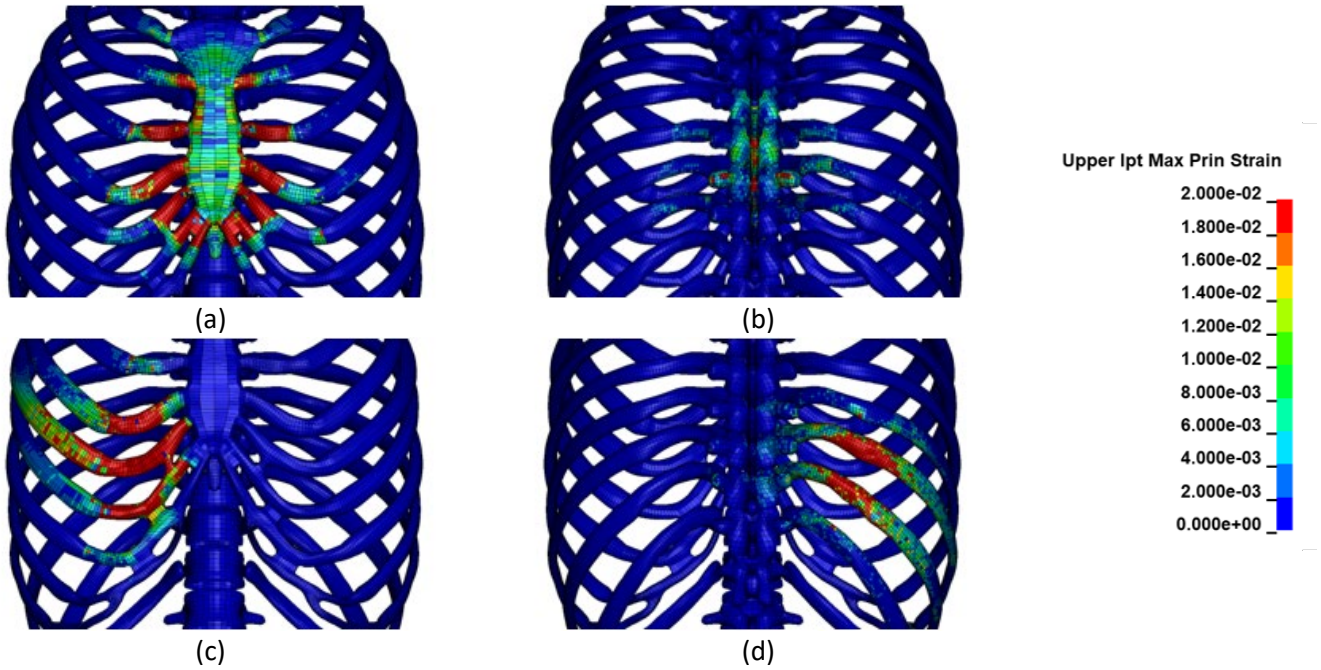

Fig. 8. Overview of maximum principal strain in the thorax at t=0.5 ms: (a) *F1*, (b) *B1*, (c) *F2* and (d) *B2*.

In general, all impact conditions had in common that elements in the ribs were significantly strained. Depending on the case, different ribs were impacted to varying extents (Table III). The highest maximum principal strains in the four most strained ribs for each case ranged from 1.01% to 1.72% for *F1,* from 1.61% to 11.93% for *F2,* from 0.85% to 3.3% for *B1,* and from 2.78% to 22.45% for *B2* (Table III). Taking a look at the results for the $VF_{1.57}$ for both centralised impact positions, it is clear that only small volumetric fraction for *F1* (≥0.04%) and for *B1* (≥0.6%) have exceeded the chosen strain threshold of 1.57% (Table III). Comparing the rib strain results of *F1* and *B1*, it seems that the ribs are more affected by the impact in the posterior case. Interestingly, for both centralised impacts the maximum strains are not observed in all of the associated rib pairs (Table III).

Looking at the $VF_{1.57}$ for the lateral impact positions over the ribs, it is obvious that significant fractions have exceeded the limit of 1.57%. For *F2* in rib *R_05* a VF of 9.94% and in *R_04* a VF of 1.19% surpassed the limit, while for *B2* the limit was exceeded in rib *R_09* with a VF of 24.53% and in *R_10* with a VF of 27.85% (Table III). The high VF values are consistent with the main areas of high rib strain in Figure 8c and Figure 8d. The comparison of the lateral positions *F2* and *B2* shows that again higher rib strains resulted in the posterior cases.

TABLE III

THE FOUR RIBS WITH THE HIGHEST MAXIMUM PRINCIPAL STRAINS AND ASSOCIATED VF(1.57%) FOR EACH POSITION

Position	**1.Rib**	**Strain [%]**	**VF [%]**	**2.Rib**	**Strain [%]**	**VF [%]**	**3.Rib**	**Strain [%]**	**VF [%]**	**4.Rib**	**Strain [%]**	**VF [%]**
F1	*R_02*	1.72	0.04	*L_04*	1.47	0.0	*L_03*	1.05	0.0	*R_04*	1.01	0.0
F2	*R_05*	11.93	9.94	*R_04*	5.2	1.19	*R_06*	3.47	0.61	*R_03*	1.61	0.02
B1	*R_09*	3.30	0.22	*R_08*	3.21	0.6	*L_09*	3.17	0.15	*R_07*	0.85	0.0
B2	*R_09*	22.45	24.53	*R_10*	11.18	27.85	*R_08*	4.76	0.34	*R_11*	2.78	0.35

The vertebrae were only analysed for the posterior cases because in the anterior impacts the spine was not significantly affected. The highest effective strains in the vertebrae could be observed for *B1*. These occurred primarily in the vertebrae *T6*, *T7* and *T8* (Table IV and Fig. 9), and were distributed mainly symmetrically due to the centralised impact. The maximum effective strains ranged from 3.68% to 13.56% in the evaluated vertebrae, while the $VF_{1.37}$ lay between 0.25% and 8.83% (Table IV and Fig. 10). The highest strain areas were located in the spinous processes and in the vertebral arch, which were caused by the bending moment (Fig. 9). Assuming that an effective strain of 1.37% would cause failure of the cortical vertebra elements, damage could be expected in the spinous processes and near the spinal canal in *T6*, *T7* and *T8*.

TABLE IV
MAXIMUM EFFECTIVE STRAINS AND VF(1.37%) IN THE VERTEBRAE T5, T6, T7, T8 AND T9 AT B1 AND B2

Vertebra	**T5**		**T6**		**T7**		**T8**		**T9**	
Position	**Strain [%]**	**VF [%]**	**Strain [%]**	**VF [%]**	**Strain [%]**	**VF [%]**	**Strain [%]**	**VF [%]**	**Strain [%]**	**VF [%]**
B1	3.68	0.26	13.56	4.62	11.78	8.58	13.52	8.83	4.05	0.25
B2	0.17	0.0	0.37	0.0	0.77	0.0	2.0	0.13	2.97	0.37

Compared to the outcome for *B1*, the impact for *B2* resulted in considerably smaller strains (Table IV and Fig. 10). The greatest maximum effective strains were determined in *T10* with a value of 3.12% and in *T9* with a value of 2.97%. Here, *T9* and *T10* were subjected to the highest amount of strains due to their anatomical contact with the associated ribs *R_09* and *R_10*, which were directly impacted for *B2*.

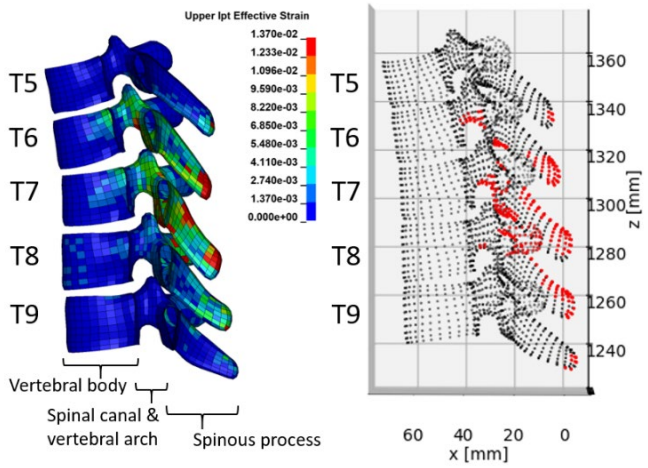

(a) (b)

Fig. 9. Cut through vertebrae *T5* to *T9* for *B1*: (a) upper integration point effective strain at t = 0.5 ms; (b) points marked in red indicate nodes whose elements have exceeded an effective strain of 1.37% at the lower or upper integration point over the total impact duration.

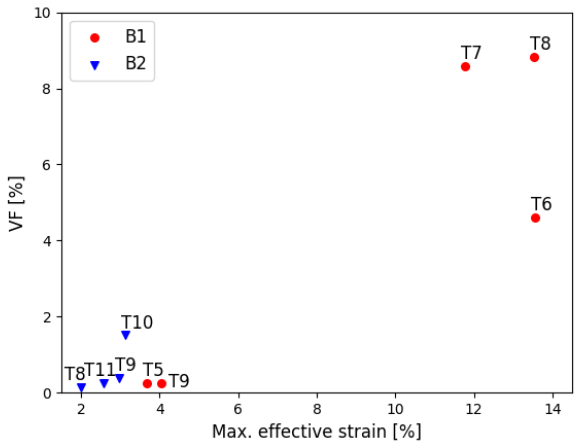

Fig. 10. $VF_{1.37}$ over maximum effective strain at *B1* and *B2* for the vertebrae with the highest strains.

IV. DISCUSSION

Depending on the impacted body position, the imprinting of a high-velocity BFD with an equal energy input resulted in different magnitudes of body wall displacements, with different internal structures being subjected to varying levels of stress. While for *B2* the smallest BWD was observed, the ribs were more heavily strained and therefore may be exposed to a higher risk of injury compared to *F2* with the highest BWD (Fig. 6 and Table III). This indicates that the safety of body armour could be improved by expanding testing standards to include consideration of specific injury tolerances of the thoracic region and not solely relying on a constant BFD limit

across the entire area of the armour [9-11].

All four positions had in common the fact that the ribs were significantly strained. Moreover, higher strains were determined in both posterior positions compared to their anterior counter positions (*B1* versus *F1*; *B2* versus *F2*). A reason for the lower strains in the anterior impact could lie in the anatomical structure of the rib cage. In the case of a frontal impact, the ribs are probably more flexible due to the connecting deformable coastal cartilage and by being jointed at the spine, resulting in smaller rib strains. This would agree with the observation of the BWD for *F2* and *B2* (Fig. 6).

Assuming that an effective strain of 1.37% would cause failure of the cortical vertebra elements, damage may occur for this specific high-velocity impact scenario in the spinous processes and near the spinal canal for *B1*, which would agree, to a certain extent, with some of the reported injuries in Table I. The value of 1.37% should be used with caution as it was determined in the event of an underbody blast, causing a different strain state than a direct horizontal impact on the spine, and also the failure strain of vertebral bodies is rate-dependent, decreasing with increasing loading rates [29-30]. Therefore, further studies are necessary to determine the fracture strain of vertebrae under high-speed horizontal impacts. A comparative analysis to the existing experimental studies is problematic due to the limited number, and especially because of the wide variation in their experimental setups (Table I). To the author's best knowledge there are no documented field cases of BABT regarding the spine. Using the GHBMC, it may be possible to predict bony injuries in the spine in the event of posterior BABT, but it is currently not possible to make any predictions about neural damage in the spinal cord, as reported by Zhang *et al*. [17].

The GHBMC has been validated for posterior blunt impacts with an impactor mass of 97.5 kg and impact velocities up to 5.5 m/s, which is below the velocity of a ballistic impact [31-32]. In order to further improve the validity of the GHBMC and other HBMs for ballistic posterior impacts, biomechanical corridors, such as those already developed by Bir *et al*. for the anterior case, would be necessary [13]. These would be of significant value for further investigations of posterior BABT.

A direct comparison of anterior and posterior BABT is challenging due to different internal structures being affected and the human body not being a homogenous entity. Nonetheless, this study highlights that it would be beneficial to consider the anterior and posterior side of the human body for the development of future thoracic region-specific injury tolerances. This study focused mainly on evaluating hard tissues in the event of BABT. Further studies should also investigate the effect on organs.

V. CONCLUSION

In this study posterior and anterior BABT were numerically analysed with the GHBMC M50-P. Two anterior impact positions (mid-sternum and 5th rib) were compared to two posterior impact positions (vertebra *T7* and between 9th and 10th rib) in regard to hard tissue strains and BWD. Using the SIL-method and adapting each impact profile individually, it was possible to investigate these impact positions with an equal energy input. Depending on the impacted body position, the imprinting of BFD with the SIL-method resulted in different magnitudes of body wall displacements, with different internal structures being subjected to varying levels of stress. The anterior impacts resulted in critical strain values in sternum, costal cartilage and ribs, while the posterior impacts resulted in critical values in ribs and vertebrae. The comparison of both posterior positions with their respective anterior positions revealed higher rib strains in both posterior cases. A direct comparison of anterior and posterior BABT is challenging due to different internal structures being affected and the human body not being a homogenous entity.

VI. ACKNOWLEDGEMENTS

We would like to express our appreciation to the Federal Office of Bundeswehr Equipment, Information Technology and In-Service Support (BAAINBw) as well as Bundeswehr Technical Center for Weapons and Ammunition (WTD 91-450) for funding this work.

VII. REFERENCES

[1] Cannon, L. (2001) Behind armour blunt trauma--an emerging problem. *Journal of the Royal Army Medical Corps*, **147**(1): pp. 87–96.

[2] Bir, C., Lance, R., Stojsih-Sherman, S., Cavanaugh, J. (2017) Behind armor blunt trauma: recreation of field cases for the assessment of backface signature testing. *Proceedings of the International Symposium on Ballistics*, 2017, Long Beach, California, United States of America.

[3] Talmy, T., Itah, A. et al. (2024) Close-Range Fire Inflicting Behind Armor Blunt Trauma: Case-Series and Implications for Battlefield Care. *Military Medicine*, **189**(1-2): pp. e448–e453.

[4] Carroll, A. W., Soderstrom, C. A. (1978) A new nonpenetrating ballistic injury. *Annals of Surgery*, **188**(6): pp. 753–757.

[5] Wilhelm, M., Bir, C. (2008) Injuries to law enforcement officers: the backface signature injury. *Forensic Science International*, **174**(1): pp. 6–11.

[6] National Institute of Justice (2008) *Ballistic Resistance of Body Armor NIJ Standard-0101.06*.

[7] National Institute of Justice (2023) *Ballistic Resistance of Body Armor NIJ Standard-0101.07*.

[8] Goldfarb, M. A., Ciurej, T. F., Weinstein, M. A., Metker, L. W. (1976) Edgewood Arsenal Aberdeen Proving Ground MD, *A method for soft body armor evaluation: medical assessment*.

[9] Hanlon, E., Gillich, P. (2012) Origin of the 44-mm behind-armor blunt trauma standard. *Military Medicine*, **177**(3): pp. 333–339.

[10] Eaton, M. A. K., Henderson, K. A., McMahon, J. A., Salzar, R. S. (2020) Testing the Validity of the NIJ Clay Standard for Approving Body Armor With a Preliminary Insight Into Injury Correlation. *Proceedings of the ASME 2020 International Mechanical Engineering Congress and Exposition*, 2020, Virtual, Online.

[11] Yoganandan, N., Shah, A. et al. (2023) A Novel Paradigm to Develop Regional Thoracoabdominal Criteria for Behind Armor Blunt Trauma Based on Original Data. *Military Medicine*, **188**(Suppl 6): pp. 598–605.

[12] Sturdivan, L. M., Viano, D. C., Champion, H. R. (2004) Analysis of injury criteria to assess chest and abdominal injury risks in blunt and ballistic impacts. *The Journal of Trauma: Injury, Infection, and Critical Care*, **56**(3): pp. 651–663.

[13] Bir, C., Viano, D., King, A. (2004) Development of biomechanical response corridors of the thorax to blunt ballistic impacts. *Journal of Biomechanics*, **37**(1): pp. 73–79.

[14] Bir, C., Viano, D. C. (2004) Design and injury assessment criteria for blunt ballistic impacts. *The Journal of Trauma: Injury, Infection, and Critical Care*, **57**(6): pp. 1218–1224.

[15] Bass, C. R., Salzar, R. S. et al. (2006) Injury risk in behind armor blunt thoracic trauma. *International Journal of Occupational Safety and Ergonomics*, **12**(4): pp. 429–442.

[16] Soderstrom, C. A., Carroll, A. W., Hawkins, C. E. (1978) Army Armament Research and Development Command Aberdeen Proving Ground MD Chemical Systems Lab, *The Medical Assessment of a New Soft Body Armor*.

[17] Zhang, B., Huang, Y. et al. (2011) Neurological, functional, and biomechanical characteristics after high-velocity behind armor blunt trauma of the spine. *The Journal of Trauma: Injury, Infection, and Critical Care*, **71**(6): pp. 1680–1688.

[18] Jennings, R. M., Malbon, C., Brock, F., Harrisson, S., Carr, D. J. (2018) A preliminary study into injuries due to non-perforating ballistic impacts into soft body armour over the spine. *Injury*, **49**(7): pp. 1251–1257.

[19] Jennings, R. M., Malbon, C., Brock, F., Harrisson, S. E., Carr, D. J. (2018) Preliminary study into the skeletal injuries sustained to the spine from posterior non-perforating ballistic impacts into body armour. *Journal of the Royal Army Medical Corps*, **164**(3): pp. 186–190.

[20] Cronin, D. S., Bustamante, M. C. et al. (2021) Assessment of Thorax Finite Element Model Response for Behind Armor Blunt Trauma Impact Loading Using an Epidemiological Database. *Journal of Biomechanical Engineering*, **143**(3).

[21] Jenerowicz, M., Matt, P. et al. (2023) Assessment of GHBMC M50-P Response for Behind Armour Blunt Trauma – Impact Loading with Approximation of 3D Surface of the Armour Back Face Displacement. *Proceedings of IRCOBI Conference*, 2023, Cambridge, United Kingdom.

[22] Bustamante, M. C., Cronin, D. S. (2024) Impact Location Dependence of Behind Armor Blunt Trauma Injury Assessed Using a Human Body Finite Element Model. *Journal of Biomechanical Engineering*, **146**(3).

[23] Klein, H., Jenerowicz, M., Trube, N., Boljen, M. (2020) How to combine 3D textile modeling with latest FE human body models. *Advances in Transdisciplinary Engineering*, (11): pp. 166–177.

[24] Boljen, M., Jenerowicz, M., Bauer, S., Straßburger, E. (2023) Combining protective clothes with human body models for finite element ballistic impact simulations. *Communications in Development and Assembling of Textile Products*, **4**(2): pp. 141–150.

[25] Gayzik, F. S., Moreno, D. P., Vavalle, N. A., Rhyne, A. C., Stitzel, J. D. (2012) Development of a Full Human Body Finite Element Model for Blunt Injury Prediction Utilizing a Multi-Modality Medical Imaging Protocol. *Proceedings of the 12th International LS-DYNA User Conference*, 2012, Detroit, United States of America.

[26] Ivanov, I., Tabiei, A. (2004) Loosely woven fabric model with viscoelastic crimped fibres for ballistic impact simulations. *International Journal for Numerical Methods in Engineering*, **61**(10): pp. 1565–1583.

[27] Viano, D. C., Lau, I. V. (1988) A viscous tolerance criterion for soft tissue injury assessment. *Journal of Biomechanics*, **21**(5): pp. 387–399.

[28] Agnew, A. M., Murach, M. M. et al. (2018) Sources of Variability in Structural Bending Response of Pediatric and Adult Human Ribs in Dynamic Frontal Impacts. *Stapp Car Crash Journal*, **62**: pp. 119–192.

[29] Somasundaram, K., Zhang, L. et al. (2019) Evaluating thoracolumbar spine response during simulated underbody blast impact using a total human body finite element model. *Journal of the Mechanical Behavior of Biomedical Materials*, **100**: pp. 103398.

[30] Kazarian, L., Graves, G. A. (1977) Compressive Strength Characteristics of the Human Vertebral Centrum. *Spine*, **2**(1): pp. 1–14.

[31] Forman, J., Perry, B. et al. (2015) Blunt impacts to the back: Biomechanical response for model development. *Journal of Biomechanics*, **48**(12): pp. 3219–3226.

[32] Zeng, W., Mukherjee, S., Caudillo, A., Forman, J., Panzer, M. B. (2021) Evaluation and Validation of Thorax Model Responses: A Hierarchical Approach to Achieve High Biofidelity for Thoracic Musculoskeletal System. *Frontiers in Bioengineering and Biotechnology*, **9**: pp. 712656.